Unsteady laminar flow between a pair of disks corotating in a fixed cylindrical enclosure

J. A. C. Humphrey, C. A. Schuler, and D. R. Webster

Articles you may be interested in

Two modes of oscillatory instability in the flow between a pair of corotating disks
Phys. Fluids **21**, 014101 (2009); 10.1063/1.3054637

Stability of flow between two corotating disks in an enclosure
Phys. Fluids **19**, 068106 (2007); 10.1063/1.2747543

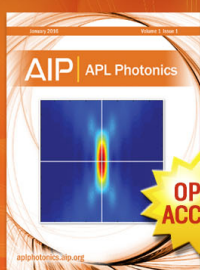Influence of the geometry on the structure of the flow between a pair of corotating disks
Phys. Fluids **11**, 88 (1999); 10.1063/1.869904

Experimental observations of an unsteady detached shear layer in enclosed corotating disk flow
Phys. Fluids A **5**, 2438 (1993); 10.1063/1.858756

The flow between shrouded corotating disks
Phys. Fluids A **1**, 241 (1989); 10.1063/1.857494

Unsteady laminar flow between a pair of disks corotating in a fixed cylindrical enclosure

J. A. C. Humphrey,[a] C. A. Schuler,[b] and D. R. Webster[c]
Department of Mechanical Engineering, Thermofluids Laboratory, University of California at Berkeley, Berkeley, California 94720-1740

The unsteady streamlined motion of a constant property fluid in the unobstructed space between a pair of disks corotating at angular velocity Ω in a fixed cylindrical enclosure is investigated numerically. Two-dimensional (axisymmetric) and three-dimensional calculations are performed using a second-order accurate time-explicit algorithm. The flow configuration corresponds to that investigated experimentally by Schuler et al. [Phys. Fluids A **2**, 1760 (1990)]. The steady flow solutions are characterized by a symmetrical pair of counter-rotating toroidal vortices in the cross-stream (r-z) plane. This secondary motion is driven by the radial imbalance between the outward-directed centrifugal force and the inward-directed pressure gradient force. Axisymmetric calculations predict a flow that is steady for Re<22 200, where Re is the Reynolds number based on the disk radius, the tip speed of the disks, and the kinematic viscosity of the fluid. Above this value the motion is unsteady periodic and, while the features of the cross-stream flow pattern are broadly preserved, the symmetry of the motion about the midplane is broken by alternating periodic crossings of the toroidal vortices. This instability is maintained through an interaction that arises between outward-directed fluid in the disk Ekman layers and inward-directed fluid in the return core flow. Three-dimensional calculations at Re=22 200 and 44 400 show that the toroidal vortices acquire a time-varying sinuous shape in the circumferential direction. These calculations reveal circumferentially periodic reversals of the axial velocity component in the cross-stream plane, including the detached shear layer separating the region of motion in solid-body rotation near the hub from the potential core, in agreement with the flow visualization observations of Humphrey and Gor [Phys. Fluids A **5**, 2438 (1993)]. The wavelength of this oscillation is shown to be twice that of the circumferential velocity component which is responsible for the nodal distribution of axial vorticity. When plotted on the interdisk midplane, the axial component of vorticity manifests itself as an even integer number, $2n$ ($n=1,2,...$), of circumferentially periodic foci. Experiments show that the number of foci decreases in a stepwise manner with increasing Reynolds number. For the conditions of this study, the calculated dimensionless angular velocity of the foci, Ω_F/Ω, ranges from 0.55 at Re=22 200 to 0.44 at Re=44 400. These values are close to the present experimental estimate $\Omega_F/\Omega=0.5$. © *1995 American Institute of Physics.*

I. INTRODUCTION

The unobstructed flow between corotating disks in a fixed cylindrical enclosure is of fundamental scientific interest and considerable practical importance to, for example, the turbomachinery, chemical reactor, and magnetic disk storage industries. Figure 1 is a schematic of the geometrical configuration of interest for which Schuler et al.[1] have identified five distinct flow regions at very large values of the Reynolds number (Re=$\Omega R_2^2/\nu$). Fluid in the Ekman layers adjacent to the disks is driven radially outward by the centrifugal force, while fluid in the core is driven radially inward along the interdisk midplane by the higher pressure at the fixed enclosure wall. The sense of rotation of the resulting average cross-stream flow is also illustrated in Fig. 1.

In earlier publications (Schuler et al.,[1] Chang et al.,[2,3] Schuler,[4] Tzeng and Fromm,[5] Humphrey et al.,[6] Tzeng and Humphrey,[7] Tzeng and Chang,[8] Humphrey et al.,[9] and Gor et al.[10]), the authors and their colleagues have extensively investigated (and reviewed) the steady flow and heat transfer of air in the unobstructed space between a pair of disks corotating in a fixed cylindrical enclosure. In contrast, except for the studies noted below, relatively little is known regarding the detailed *three-dimensional* structure of the *unsteady* flow in this configuration.

A. Unsteady flow between corotating disks

1. Experimental work

Lennemann[11] and Akhmetov and Tarasov[12] visualized the unsteady flow of water between a pair of enclosed corotating disks, and observed that the inner flow region in solid-body rotation is circular for low Reynolds number. As the Reynolds number is increased, the axisymmetric character of the motion is lost and the interface demarcating the inner flow region acquires an unsteady polygonal shape. Subsequently, Abrahamson et al.[13,14] used bromothymol blue indi-

---

[a] Author to whom correspondence should be addressed; Department of Aerospace and Mechanical Engineering, University of Arizona, Tucson, Arizona 85721, Phone: 520-621-2236.
[b] Present address: Aerometrics, Inc., 550 Del Rey Avenue, Sunnyvale, California 94086.
[c] Present address: Department of Mechanical Engineering, Stanford University, Stanford, California 94305.
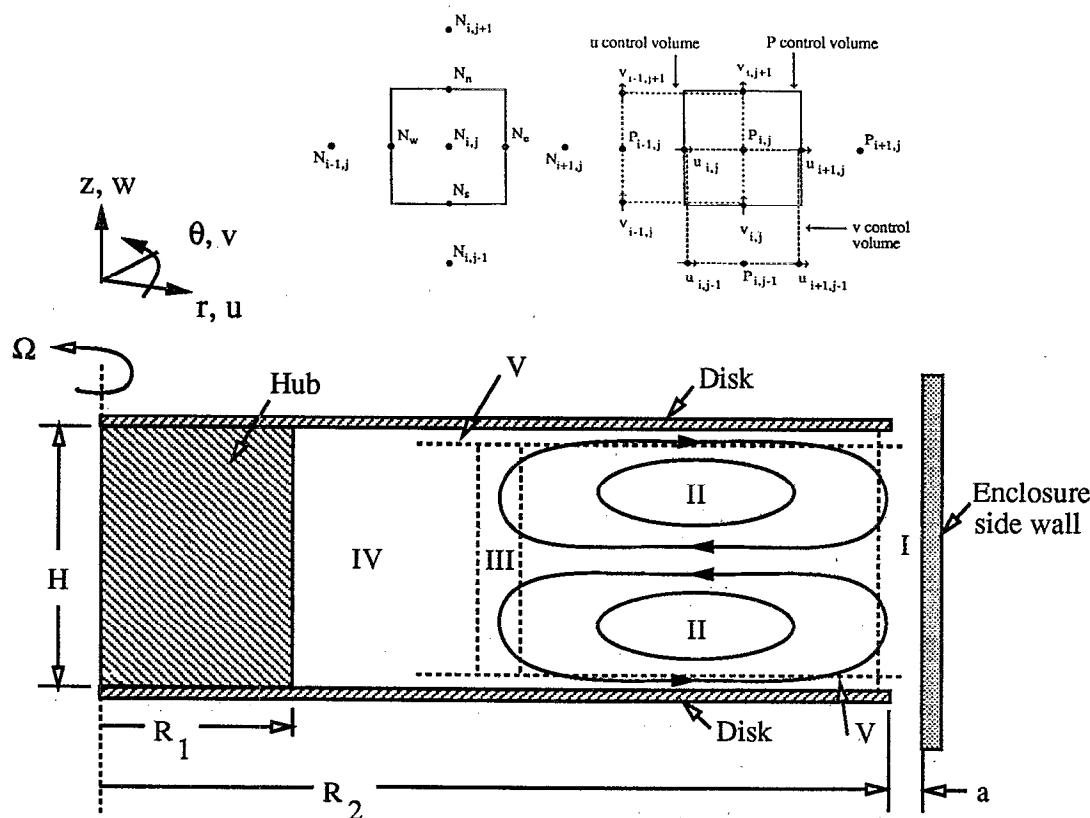
FIG. 1. Schematic of the corotating disk flow configuration indicating the toroidal vortices that develop in the cross-stream plane near the fixed enclosure wall. Also shown are the flow regions established through scaling considerations by Schuler et al.:[1] (I) enclosure wall boundary layer; (II) core potential flow; (III) detached shear layer; (IV) the region in solid-body rotation; (V) disk Ekman layers. The insert shows a typical two-dimensional $(r\text{-}\theta)$ projection and node labeling of adjoining velocity (components u and v) and scalar (pressure P) control volumes on the staggered calculation grid.

cator dye and the hydrogen bubble technique to visualize the flow of water in an apparatus geometrically and dynamically similar to that of Lennemann. From their observations, the flow field between a pair of disks is divided into three distinct regions: an inner region, an outer region, and a boundary layer region adjacent to the enclosure wall. As in Lennemann's study, for the case of an unobstructed flow, the inner region is observed to move in solid body rotation. The authors also noted the presence of an integer number of circumferentially periodic vortices aligned in the axial (z-coordinate) direction in the outer region, near the enclosure wall, rotating at roughly 75% of the angular velocity of the disks. Although not measured, the strength of these vortices is qualitatively judged to increase with increased disk spacing and increased rotation rate. The number of vortices is observed to decrease with increased disk spacing and increased rotation rate.

Schuler et al.[1,4] measured radial and axial profiles of the mean and rms circumferential velocity component with a laser-Doppler velocimeter for the axisymmetric air flow configuration of Fig. 1 with $R_1 = 56.4$ mm, $R_2 = 105$ mm, $H = 9.53$ mm, and $a = 2.7$ mm. Time-resolved measurements of the circumferential velocity component were also obtained along the interdisk midplane for values of Re ranging from 4440 to 281 200 (Ω_r ranging from 60 to 3800 rpm). These data reveal a transition from steady axisymmetric mo-

tion to unsteady three-dimensional (nonaxisymmetric) motion between Re=4440 and 4740 ($\Omega_r = 60$ and 64 rpm). The transition is marked by relatively large increases in the rms velocity over extended regions of the flow, even though the corresponding distributions of dimensionless mean velocity remain essentially unchanged. For Re>4440, the velocity time records display distinct sinusoidal-like oscillations, with the corresponding spectra revealing energetic peaks at well-defined frequencies.

It is believed that the velocity oscillations observed by Schuler[4] are linked to the presence of circumferentially periodic foci of intensified axial vorticity of the type observed in the earlier visualization experiments. A plot of the Strouhal number, St=$60f/\Omega_r$, associated with the velocity oscillations is shown in Fig. 2 as a function of Re. The data are from Schuler[4] and were measured at $r/R_2 = 0.895$ on the interdisk midplane. In the definition of St, f is the frequency in Hz of the circumferential velocity component measured with respect to a fixed frame of reference, and Ω_r is the disk speed of rotation in rpm. The measurements reveal a staircase pattern, wherein the value of f is always nearly an integer multiple of the disk rotation frequency over the entire range of Re. The values of Re marking the transitions in St are sharply defined. The staircase pattern is in qualitative agreement with the flow visualization results of Abrahamson et al.[13,14] It suggests that if the velocity oscillations are due
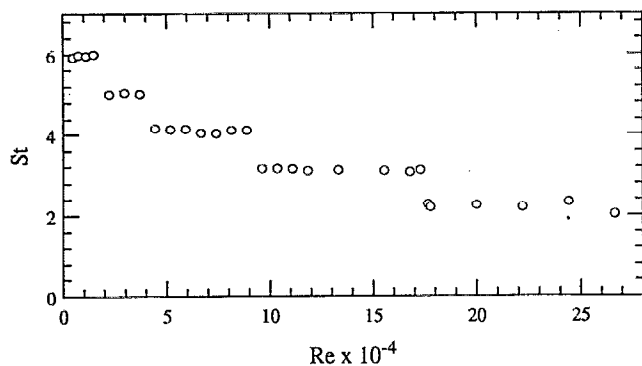
FIG. 2. Dimensionless oscillation frequency of the circumferential velocity component, St, versus Reynolds number, Re, measured at $r/R_2 = 0.895$ on the interdisk midplane. The data correspond to the case of increasing disk speed of rotation.

to the periodic passage of foci of axial vorticity distributed in the circumferential direction, and if the foci rotate at a fixed fraction of the disk angular velocity, then their number is decreasing in a stepwise manner with increasing disk speed of rotation. The numerical findings of the present work support this interpretation.

The data in Fig. 2 were obtained by gradually increasing the angular velocity of the disks in the enclosure. A hysteresis in the measured values of Re at which the transitions in St occurred was observed by Schuler[4] when the system was brought to the target speed of rotation from a higher value. The transition values of Re were observed to decrease by about 20% when the angular velocity of the disks was gradually decelerated, compared to the values obtained when it was accelerated. The experimental evidence is that the flow patterns observed for accelerating conditions are more stable than those observed for decelerating conditions.

By illuminating micron-sized mineral oil droplets with a sheet of laser light, Humphrey and Gor[15] visualized the cross-stream flow in the experimental apparatus of Schuler et al.[1,4] Their measurements confirm theoretical relations derived by Schuler[4] for the location and thickness of the detached shear layer (region III in Fig. 1). These authors also document the critical Re for the detached shear layer to become unsteady, and suggest a connection between the onset of flow unsteadiness and the appearance of the circumferentially distributed foci of intensified axial vorticity. Again, present numerical findings support this interpretation.

2. Numerical work

Direct numerical simulations of the two-dimensional (axisymmetric) unsteady flow between a pair of unobstructed corotating disks with very small aspect ratio ($H/R_2 \ll 1$) have been performed by Fromm,[16,17] who investigated the stability characteristics of the motion and its transition to turbulence in the absence of an enclosure. This configuration represents a limiting case of the present one where shearing of the flow by the fixed curved enclosure wall plays a dominant role in establishing the characteristics of the secondary motion. Tzeng and Fromm[5] later performed axisymmetric

numerical calculations of the unsteady flow associated with four disks corotating in a fixed cylindrical enclosure. Memory and computer time constraints limited the number of grid nodes in the space between any pair of disks to 16 in the axial direction and 20 in the radial direction. This relatively coarse grid resulted in large discrepancies between the calculated and measured rms velocity distributions, and a larger value of Re for transition to the unsteady flow regime relative to the experiments.

In these numerical studies the unsteady flow was assumed to be axisymmetric, even throughout the laminar/turbulent transition regime. However, experimental and numerical evidence now available for disks rotating in enclosures, discussed further below, shows that transition from axisymmetric steady laminar flow to three-dimensional unsteady laminar flow precedes the laminar/turbulent flow transition. This limits, therefore, the insight that can be gained from an analysis of the above and similar numerical solutions, since it is unclear what the relation is of these solutions to the experimental results.

B. The present contribution

The objective of this study is to investigate the structure and field dynamics of the isothermal flow of air in the unobstructed space between a pair of disks corotating in a fixed cylindrical enclosure. Two- and three-dimensional calculations are performed with the numerical procedure of Schuler et al.[18] for a range of Re in which, although unsteady, the flow is not turbulent. The target for the numerical calculations is the flow configuration shown in Fig. 1 for the dimensions and conditions mentioned above, in relation to the investigations of Schuler et al.[1,4] Although quantitatively imperfect due to unavoidable numerical diffusion, the calculations allow a much improved, and hitherto undocumented, qualitative understanding of this complex class of flows, especially when interpreted together with the experimental data available. In particular, as will be shown, the calculations help explain noteworthy differences observed among earlier experimental investigations as a result of variations in experimental conditions and/or measurement procedures.

II. THE NUMERICAL PROCEDURE

The numerical procedure used to calculate the present flow, CUTEFLOWS (Computing Unsteady Three-dimensional Elliptic Flows), originates in the implicit finite-difference algorithm originally developed by LeQuere et al.,[19] subsequently improved by Arnal et al.[20] and Schuler et al.[4,18] It solves directly for the primitive flow variables (velocity and pressure) on a staggered grid configuration. Thus, in addition to the velocity components, the pressure field must be calculated at every time step in order to enforce continuity. The present account is the first comprehensive summary of the numerical procedure. For complete details the reader is referred to Schuler et al.[4,18]

A. Conservation equations and boundary conditions

With reference to Fig. 1, the equations describing the unsteady motion of a constant property fluid relative to a fixed frame of reference in cylindrical coordinates are the following: Continuity,

$$(ru)_{,r} + v_{,\theta} + rw_{,z} = 0;\tag{1}$$

r momentum,

$$\rho[u_{,t} + \nabla \cdot (\mathbf{u}u)] = \mu\,\nabla^2 u - \mu\left(\frac{2v_{,\theta}+u}{r^2}\right) - p_{,r} + \frac{\rho v^2}{r};\tag{2}$$

θ momentum,

$$\rho[v_{,t} + \nabla \cdot (\mathbf{u}v)] = \mu\,\nabla^2 v + \mu\left(\frac{2u_{,\theta}-v}{r^2}\right) - \frac{1}{r}\,p_{,\theta}$$

$$- \frac{\rho u v}{r};\tag{3}$$

and z momentum

$$\rho[w_{,t} + \nabla \cdot (\mathbf{u}w)] = \mu\,\nabla^2 w - p_{,z},\tag{4}$$

where u, v, and w are the three velocity components in the r, θ, and z coordinate directions, respectively; p is the pressure; ρ and μ are the fluid density and dynamic viscosity, respectively; ∇ is the gradient operator; ∇^2 is the Laplacian operator; and the subindices after a comma denote partial differentiation. The equations are written in dimensional form, since, as shown in Schuler et al.,[1] the appropriate length scales to nondimensionalize them depend upon the region of flow under consideration.

With reference to Fig. 1, the boundary conditions are as follows. At the hub and disk surfaces the no-slip condition requires that $u = w = 0$ and $v = \Omega r$. At the fixed curved enclosure surface, $u = v = w = 0$. Assuming the thickness of the disks to be negligible, in the gap between a disk edge and the enclosure wall, the symmetry condition $(\partial u/\partial z = \partial v/\partial z = w = 0)$ is imposed. For the three-dimensional calculations the solution is required to be periodic in the circumferential coordinate direction with a period equal to 2π.

B. Finite difference approximations

The staggered grid control-volume approach, extensively discussed by Patankar,[21] is used to derive finite difference approximations to the conservation equations and boundary conditions. This is similar to the MAC scheme proposed earlier by Harlow and Welch.[22] The calculation domain is subdivided into control volumes centered on the main grid nodes, where scalar quantities, like pressure, are stored. In contrast, the three velocity components are respectively stored at grid locations which are staggered with respect to the main scalar grid nodes. The insert in Fig. 1 shows a typical two-dimensional projection of staggered velocity and scalar control volumes. The staggered grid arrangement avoids the problem of decoupled velocity and pressure fields that can arise on nonstaggered grids.

Equations (2)–(4) can be written in the general form:

$$\rho[\psi_{,t} + \nabla \cdot (\mathbf{u}\psi)] = \mu\nabla^2 \cdot \nabla^2 \psi + S_{\psi d} + S_{\psi c} + S_{\psi p},\tag{5}$$

TABLE I. Source terms.

Equation	$S_{\psi p}$	$S_{\psi d}$	$S_{\psi c}$
r momentum	$-\dfrac{\partial p}{\partial r}$	$-\mu\left(\dfrac{2v_{,\theta}+u}{r^2}\right)$	$\dfrac{\rho v^2}{r}$
θ momentum	$-\dfrac{1}{r}\dfrac{\partial p}{\partial \theta}$	$\mu\left(\dfrac{2u_{,\theta}-v}{r^2}\right)$	$-\dfrac{\rho u v}{r}$
z momentum	$-\dfrac{\partial p}{\partial z}$	0	0

where ψ is any of u, v, or w; $S_{\psi d}$ and $S_{\psi c}$ represent the diffusion and acceleration source terms that arise in cylindrical coordinates; $S_{\psi p}$ is the pressure gradient source term. Table I summarizes the forms of the source terms in cylindrical coordinates.

Finite difference forms of the momentum equations are obtained by integration of Eq. (5) over the appropriate velocity component control volume. The detailed derivation is available in Schuler.[4] The result is

$$\rho\,\Delta V^\psi \psi_{P,t} + C_e^\psi \psi_e - C_w^\psi \psi_w + C_n^\psi \psi_n - C_s^\psi \psi_s + C_d^\psi \psi_d - C_u^\psi \psi_u$$

$$= \overline{S_\psi}\,\Delta V^\psi + \Pi_\psi + \mu\left[\left(A^\psi \frac{\partial \psi}{\partial r}\right)_e - \left(A^\psi \frac{\partial \psi}{\partial r}\right)_w\right.$$

$$+ \left(A^\psi \frac{1}{r} \frac{\partial \psi}{\partial \theta}\right)_n - \left(A^\psi \frac{1}{r} \frac{\partial \psi}{\partial \theta}\right)_s + \left(A^\psi \frac{\partial \psi}{\partial z}\right)_d$$

$$\left. - \left(A^\psi \frac{\partial \psi}{\partial z}\right)_u\right].\tag{6}$$

In this expression, the value ψ_P (for example, u_p in the insert in Fig. 1) is constant throughout the control volume centered at P. Quantities subscripted by u, d, n, s, e, and w are evaluated at the control volume surfaces denoted by these subindices. The same integration procedure when applied to the continuity Eq. (1) over a scalar control volume yields

$$C_e^\psi - C_w^\psi + C_n^\psi - C_s^\psi + C_d^\psi - C_u^\psi = 0,\tag{7}$$

where the superscript ψ now refers to the pressure variable, p.

In Eqs. (6) and (7), the following definitions apply:

$$C_e^\psi = (A^\psi \rho u)_e, \quad C_w^\psi = (A^\psi \rho u)_w,$$

$$C_n^\psi = (A^\psi \rho v)_n, \quad C_s^\psi = (A^\psi \rho v)_s,$$

$$C_d^\psi = (A^\psi \rho w)_d, \quad C_u^\psi = (A^\psi \rho w)_u,$$

$$\overline{S_\psi} = \frac{1}{\Delta V^\psi} \int_{\Delta V^\psi} (S_{\psi d} + S_{\psi c})\,dV,$$

where the symbol $(A^\psi)_i$ represents the area of the i face of the ψ control volume, and ΔV^ψ is its volume. The integrated pressure term, Π_ψ, is given in Table II for each component of momentum.

Second-order accurate central differencing is used to approximate the diffusion terms in Eq. (6). The values of advected quantities at the surfaces of a control volume are expressed in terms of the values for these quantities at the

TABLE II. Discretized pressure source terms.

Equation	Π_ψ
r momentum	$A^u_e p_P - A^u_w p_W$
θ momentum	$A^v_n p_P - A^v_s p_S$
z momentum	$A^w_d p_P - A^w_u p_U$

adjacent nodal points using the upstream-weighted second-order accurate QUICK scheme proposed by Leonard.[23] With these approximations, Eq. (6) becomes an ordinary differential equation in time for ψ_P in terms of its surrounding values and the appropriate pressure differences.

C. Time-marching solution methodology

The time marching scheme employed in this work follows closely the ideas proposed by Chorin[24] and Chorin and Mardsen,[25] who decompose the divergence-free vector velocity field into two parts according to the form $\mathbf{u} = \hat{\mathbf{u}} + \nabla \pi$, where $\nabla \pi$ is the pressure contribution to $\mathbf{u}$ over a time interval Δt. In this scheme, the pseudovelocity field $\hat{\mathbf{u}}$ is computed by explicitly advancing the time integration of the discretized momentum equations from time t to $t + \Delta t$, ignoring the (temporarily unknown) pressure contribution to the momentum balance in the interval $(t, t + \Delta t)$.

To obtain a divergence-free velocity field at time $t + \Delta t$, the pressure contribution to the momentum balance must be accounted for. A discretized pressure equation is constructed by substituting the momentum equations, discretized both in space and time, into the discretized continuity, Eq. (7). This results in a system of algebraic equations for pressure in which the nonhomogeneous terms are a function of the calculated $\hat{\mathbf{u}}$ values. Once this system is solved and the pressure field obtained, the pressure contributions to each of the momentum equations is computed and added to the $\hat{\mathbf{u}}$ field to yield the velocity field $\mathbf{u}$ at time $t + \Delta t$. The latter quantity now satisfies both the continuity and momentum balances.

The details of this approach are as follows. The spatially discretized momentum balance, Eq. (6), is first written as

$$\rho \, \Delta V^\psi \psi_{P,t} = \hat{g}_P(\psi) + \Pi_\psi, \tag{8}$$

where $\hat{g}_P(\psi)$ includes all the contributions to the balance, except for the pressure forces that are contained in Π_ψ. Following the ideas presented above, Eq. (8) is used to construct the following second-order predictor–corrector algorithm.

STEP 1: Compute the predictor-step pseudovelocities at time $n + \frac{1}{2}$, ignoring the pressure contribution to the momentum balance:

$$\hat{\psi}_P^{n+1/2} = \psi_P^n + \frac{C \, \Delta t}{\rho \, \Delta V^\psi} \hat{g}_P(\psi^n). \tag{9}$$

STEP 2: Compute the predictor-step pressure field at time n, p^n, by solving the appropriate system of algebraic equations that enforces the continuity (divergence-free) constraint upon the intermediate velocity field $\psi_P^{n+1/2}$.

STEP 3: Compute the predictor-step velocities according to

$$\psi_P^{n+1/2} = \hat{\psi}_P^{n+1/2} + \frac{C \, \Delta t \, \Pi_\psi^n}{\rho \, \Delta V^\psi}. \tag{10}$$

STEP 4: Compute the corrector-step pseudovelocities at time $n + 1$, ignoring the pressure contribution to the momentum balance:

$$\hat{\psi}_P^{n+1} = \psi_P^n + \frac{C \, \Delta t}{\rho \, \Delta V^\psi} \hat{g}_P(\psi^{n+1/2}). \tag{11}$$

STEP 5: Compute the corrector-step pressure field at time $n + \frac{1}{2}$, $p^{n+1/2}$, by solving the appropriate system of algebraic equations that enforces the continuity (divergence-free) constraint upon the new velocity field ψ_P^{n+1}.

STEP 6: Compute the predictor-step velocities, according to

$$\psi_P^{n+1} = \hat{\psi}_P^{n+1} + \frac{C \, \Delta t \, \Pi_\psi^{n+1/2}}{\rho \, \Delta V^\psi}, \tag{12}$$

where $C = \frac{1}{2}$ for the predictor steps and $C = 1$ for the corrector steps.

D. The pressure equation and solution procedure

The pressure equations required in Steps 2 and 5 of the algorithm result from combining Eq. (7) with Eqs. (10) and (12), respectively. For the staggered grid employed, this procedure leads to

$$a_P p_P^{n+C-1/2} = a_E p_E^{n+C-1/2} + a_W p_W^{n+C-1/2} + a_N p_N^{n+C-1/2}$$
$$+ a_S p_S^{n+C-1/2} + a_D p_D^{n+C-1/2}$$
$$+ a_U p_U^{n+C-1/2} + S_P^{n+C}, \tag{13}$$

where

$$a_P = a_E + a_W + a_N + a_S + a_D + a_U,$$

$$a_E = \frac{\Delta t \, A_e^P A_{ee}^u}{\Delta V^u{}_E}, \quad a_W = \frac{\Delta t \, A_w^P A_w^u}{\Delta V^u{}_P},$$

$$a_N = \frac{\Delta t \, A_n^P A_{nn}^v}{\Delta V^v{}_N}, \quad a_S = \frac{\Delta t \, A_s^P A_s^v}{\Delta V^v{}_P},$$

$$a_D = \frac{\Delta t \, A_d^P A_{dd}^w}{\Delta V^w{}_D}, \quad a_U = \frac{\Delta t \, A_u^P A_u^w}{\Delta V^w{}_P},$$

$$S_P^{n+C} = (\rho/C)(-A_e^P \hat{u}_E^{n+C} + A_w^P \hat{u}_P^{n+C} - A_n^P \hat{v}_N^{n+C} + A_s^P \hat{v}_P^{n+C}$$
$$- A_d^P \hat{w}_D^{n+C} + A_u^P \hat{w}_P^{n+C}),$$

with $C = \frac{1}{2}$ and 1 for the predictor (Step 2) and corrector (Step 5) steps, respectively. The double subscripts ee, nn, and dd denote the east, north, and downstream surfaces of the staggered velocity control volumes for the u, v, and w velocity components located at the e, n, and d faces of a scalar (nonstaggered) control volume.

Some implementation notes are in order: (i) The predictor and corrector formulas differ only by the value of the constant C. Thus, the same code can be used for both. (ii) Once the right-hand side of Eq. (11) has been evaluated, $\psi^{n+1/2}$ is no longer needed. Thus, the same computer storage locations can be used for $\psi^{n+1/2}$ and ψ^{n+1}. (iii) The coeffi-

cients of Eq. (13) do not depend on the velocity field and need be evaluated only once, at the beginning of the computation. Only the source terms must be updated at each new time step. (iv) Since the procedure is explicit, no underrelaxation factors are required. This is in contrast with implicit time-marching schemes, where changes in the dependent variables have to be modulated from iteration to iteration within a time step to achieve convergence. The explicit approach also obviates the need for recalculating and periodically regrouping the source terms.

The solution of Eq. (13) can be obtained by direct matrix inversion, but would require huge storage resources. Consequently, an alternative iterative solution procedure is desirable. The conjugate-gradient method, originally conceived to solve unconstrained nonlinear optimization problems, can be applied to solve algebraic equations generated by finite-difference approximations, like Eq. (13). Khosla and Rubin[26] show, for finite-differenced Laplace equations, that the conjugate-gradient method converges to a solution at a rate one order of magnitude faster than those for the more commonly used point successive relaxation, successive line relaxation, and alternating direction implicit algorithms, or the strongly implicit procedure of Stone.[27] Similar improvements were noted by Kershaw.[28] In particular, since the method only employs vector multiplication and addition operations, it is attractive when parallel/vector computers are employed because its implementation parallelizes and vectorizes fully.

The derivation and the convergence properties of the conjugate-gradient method are given in Luenberger.[29] The iterative solution technique is equivalent to using the Gramm–Schmidt orthogonalization process to form sequences of orthogonal vectors with respect to the coefficient matrix (see Peyret and Taylor[30]). In order for the method to converge to a solution, the coefficient matrix operating on the pressure vector must be symmetric and positive definite. It can be shown for a two-dimensional, uniform grid that the coefficient matrix corresponding to Eq. (13) satisfies these two properties. Although we have not been able to prove that the matrix is positive definite in the general case, the algorithm works successfully.

A simple way to assess the convergence of the numerical solution at any given iteration is to monitor the values of the total mass residual. In CUTEFLOWS, for each time step, the iteration sequence is halted when the magnitude of this residual falls below a preset value. In addition, time sequences of calculated point values of velocity and integral values of, for example, circulation, are useful for establishing the presence of a steady or a steady-periodic solution.

Full details concerning the theory and practical implementation of the numerical procedure are contained in the works of Schuler et al.[4,18] These references contain numerous rigorous tests, including the calculation of two-dimensional unsteady bluff body flows[31,32] and selected rotating disk flows.[33] In addition, the algorithm correctly calculates a backward-facing step benchmark problem established for isothermal[34] and nonisothermal[35] flow conditions. These tests provide preliminary estimates of the grid spacing
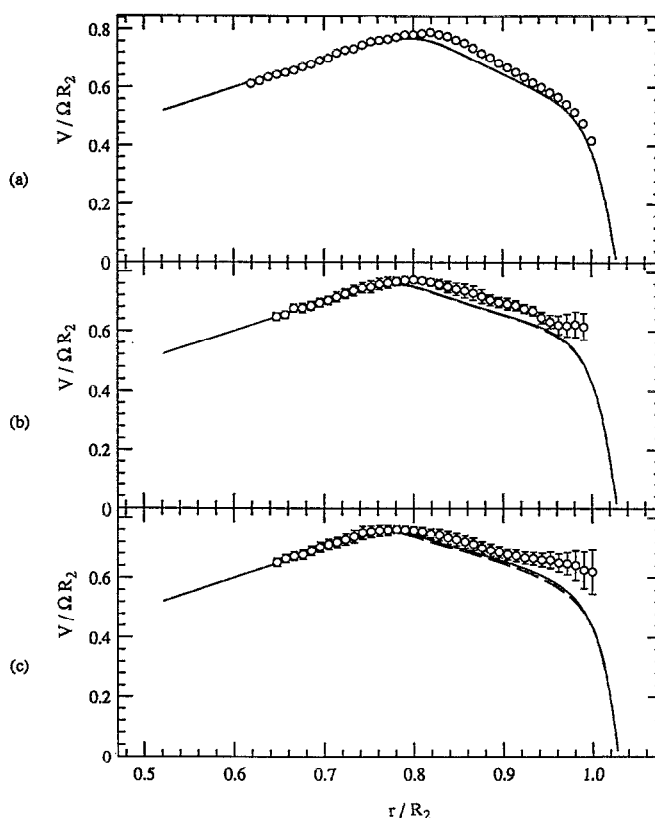

FIG. 3. Comparison between measurements (circles) and two-dimensional calculations (lines) of the circumferential velocity component along the interdisk midplane for (a) Re=4440 (60 rpm), (b) 7400 (100 rpm), and (c) 14 800 (200 rpm). The lengths of the vertical bars are twice the experimental rms at each location. (---) 31×41 grid; (—) 61×82 grid. The results for the two grids virtually coincide.

and time step sizes necessary to obtain numerical results of the accuracy required for the present study.

III. NUMERICAL RESULTS AND DISCUSSION

In the plots presented in this section, the symbols u, v, w, ω_θ, and ω_z denote instantaneous quantities, while the symbols V and $\tilde{V}$ denote the time average and rms of v, respectively.

A. Steady two-dimensional flow

Calculations are first performed assuming two-dimensional (axisymmetric) flow in the configuration of Fig. 1 for conditions of the experiment of Schuler et al.,[1,4] described in Section I A 1. Radial profiles of the circumferential velocity component calculated on the interdisk midplane for Re=4440, 7400, and 14 800 ($\Omega_r=60$, 100, and 200 rpm), are compared in Fig. 3 with the experimental data of Schuler.[4] The calculations are performed using two nonuniform grids of 31×41 and 61×82 ($n_r \times n_z$) nodes. Nonuniform grid spacing ensured the necessary refinement to resolve the steep velocity gradients arising next to the disks and the fixed enclosure wall. The calculations are started from a zero initial velocity condition, and allowed to evolve in time until the steady-state solution is reached. A time step

of 10^{-4} s is used after showing that smaller time steps have a negligible effect on the results. The predictions vary insignificantly between the two grids, with only slight differences arising in the range $0.8<r/R_2<0.96$ for the case with Re $=14\,800$. Notwithstanding, the remaining two-dimensional calculations reported here correspond to the finer 61×82 grid.

The agreement between the measurements and the calculations in Fig. 3 is very good at all the midplane radial locations for the lowest rotation rate. For Re=7400 and 14 800, the agreement is also good, except near the enclosure wall. The differences there are explained by noting that in the experiment the flow is unsteady and periodic in time for Re>4440. The vertical bars superimposed on the experimental data in Fig. 3 are twice the measured rms of the circumferential velocity. As shown below, the numerical procedure predicts unsteady two-dimensional flow for Re>22 200 ($\Omega_r>300$ rpm). These unsteady results yield radial midplane profiles of the mean circumferential velocity component with proportionately larger values near the enclosure wall; the increase in velocity being of the order of the calculated rms. When the interdisk flow oscillates, whether in the experiments or in the calculations, a velocity "sensor" located on the midplane near the enclosure wall will register periodic increases of the local circumferential velocity due to alternating axial displacements of the flow across the midplane. This yields a time-averaged value of circumferential velocity larger than that observed in a corresponding steady flow. (Note that when the experimentally determined rms value is added to each of the calculated points in Fig. 3, the resulting velocity profiles are in much better agreement with the measured results.)

Figure 4 shows contours of the circumferential vorticity component, ω_θ, in the cross-stream ($r-z$) plane for the speeds of rotation of Fig. 3. In accordance with the scaling analysis of Schuler et al.,[1] the vorticity is nondimensionalized by $\Omega\,\mathrm{Re}^{-1/2}$. In the figure, the hub is the left boundary, the enclosure wall is the right boundary, and the disks are the top and bottom boundaries of each of the three inserts. The structure of the flow is remarkably similar to that predicted analytically by Schuler et al.[1] employing zonal scaling analysis and dimensional considerations in the limit Re→∞. An Ekman layer develops along the surface of each disk, starting at the radial location where the circumferential velocity profile first deviates from solid-body rotation (see Fig. 3). Analysis shows that the thickness of an Ekman layer, marked by an arrow in each insert, is of order $\delta_E=(\nu/\Omega)^{1/2}$ and uniform. The fluid forced radially outward in the Ekman layers is redirected in the axial direction along the enclosure wall, and then radially inward into the core of the flow about the interdisk midplane, thus creating a pair of symmetrical, toroidally shaped, counter-rotating vortices. A thin shear layer with thickness also of order δ_E develops very near the fixed enclosure wall. The numerically calculated Ekman layer thicknesses are nearly uniform with r, and in agreement with the above estimate for δ_E obtained by Schuler et al.[1] The basic structure of the flow is relatively independent of the Reynolds number, also in agreement with the
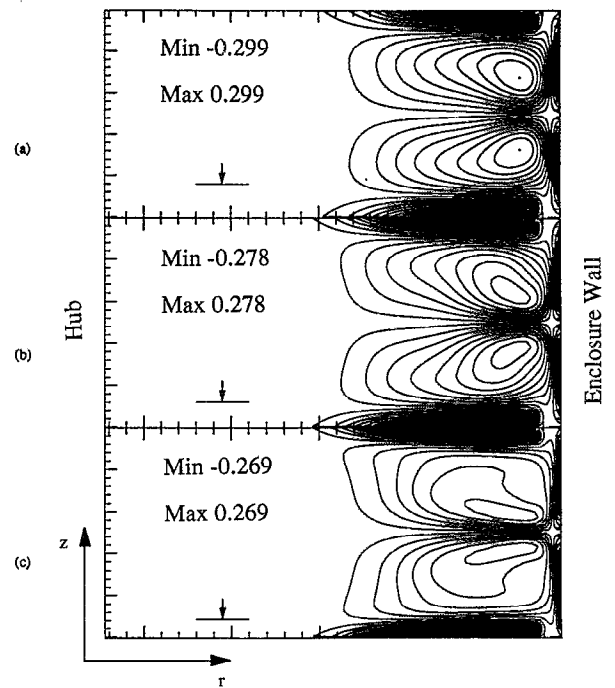

FIG. 4. Isocontours of the circumferential vorticity component, $\omega_\theta/\Omega\,\mathrm{Re}^{-1/2}$, obtained from two-dimensional calculations for (a) Re=4400, (b) 7400, and (c) 14 800. There are 40 isocontours drawn between the minimum and maximum values shown. In this and subsequent figures, an arrow marks the thickness of an Ekman layer, estimated according to $\delta_E=(\nu/\Omega)^{1/2}$.

predictions of the theoretical analysis presented in that reference.

B. Unsteady periodic two-dimensional flow

Axisymmetric numerical calculations were also performed for Re=22 200, using as the initial condition at $t=0$ the steady solution obtained for Re=14 800. This is equivalent to imposing a stepwise velocity change in the flow. A stable steady-state solution could not be obtained at this higher rate of rotation. Plots of the circumferential vorticity component provided in Fig. 5(a) show that the flow initially evolves to form two nearly symmetrical toroidal vortices in the region near the enclosure wall, similar in appearance to the steady-state vortices predicted at the lower rotation rates. However, with time the midplane symmetry of this counter-rotating pair is broken. The stagnation point where the two opposing axially directed flows meet along the fixed enclosure wall no longer coincides with the geometrical symmetry plane, but starts oscillating about it. The oscillations grow quickly and a constant amplitude oscillatory cross-stream motion is established with a flow pattern that alternates in time between the extreme states shown in Figs. 5(b) and 5(c).

Figure 6 shows the corresponding contours of the circumferential velocity component. The inward-directed radial jet flowing along the interdisk midplane convects fluid with small circumferential momentum from the enclosure wall region into the core of the flow. This creates large axial gradients of the circumferential velocity component in this region
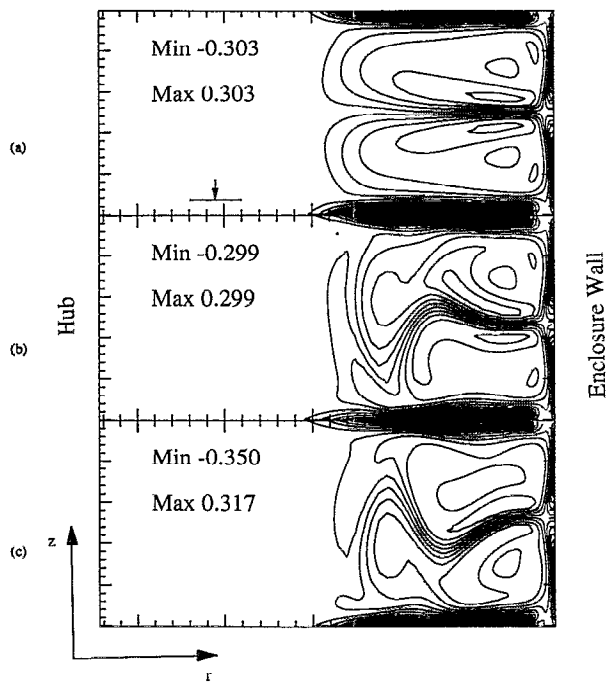
FIG. 5. Isocontours of the circumferential vorticity component, $\omega_\theta/\Omega\,\mathrm{Re}^{-1/2}$, obtained from two-dimensional calculations for Re=22 200 (300 rpm) at (a) $\Omega_r t/60=5$, (b) 13.75, and (c) 17.5. There are 40 isocontours drawn between the minimum and maximum values shown.
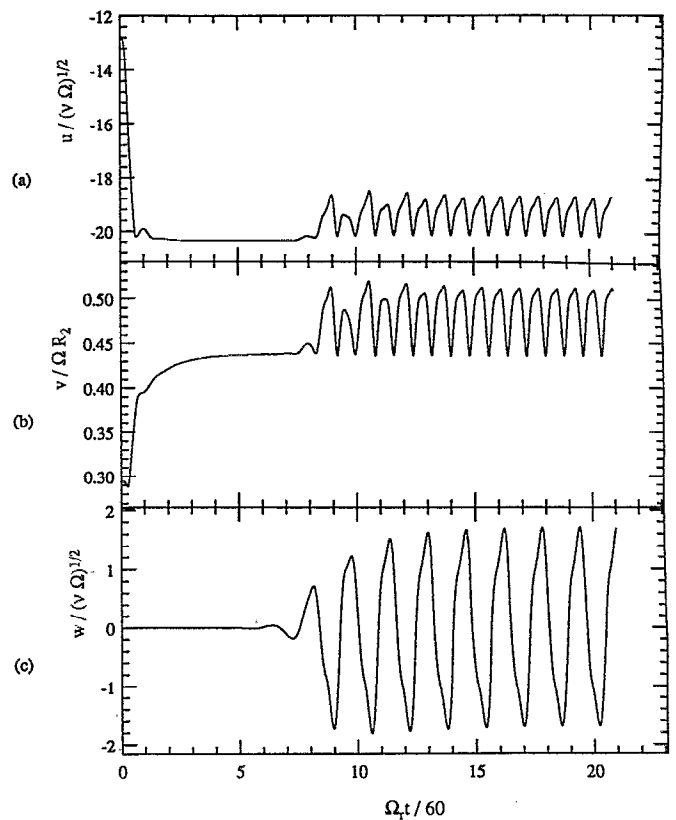

FIG. 7. Time variation of the three velocity components at $r/R_2=1$ on the interdisk midplane, obtained from two-dimensional calculations for Re =22 200. Note the two velocity scales used for nondimensionalization.

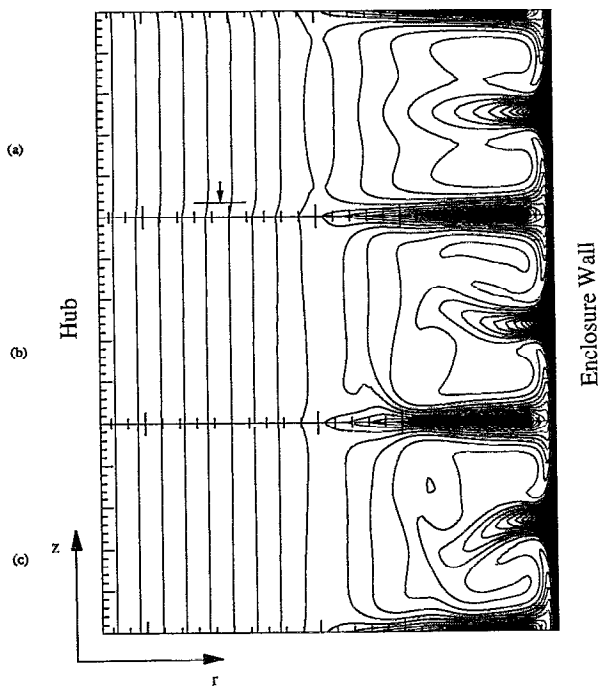FIG. 6. Isocontours of the circumferential velocity component, $v/\Omega R_2$, obtained from two-dimensional calculations for Re=22 200 at (a) $\Omega_r t/60=5$, (b) 13.75, and (c) 17.5. There are 40 isocontours drawn between $v/\Omega R_2=0$ and 1.

of the flow [see Fig. 6(a)]. Once the cross-stream flow oscillations are established, they induce periodic axial displacements of the inward-directed jet [see Figs. 6(b) and 6(c)]. A velocity sensor fixed in space at a location on the midplane between the disks near the enclosure wall would be exposed to fluid with alternating high and low circumferential velocity [see Fig. 7(b)]. Since the geometry is symmetrical with respect to the midplane, the perturbation induced in the circumferential velocity component by the periodic axial displacement of the jet is the same (and always positive) when the jet moves upward as when it moves downward.

Figures 5 and 6 show that the amplitude of the periodic axial displacement of the return jet flow increases as the radius decreases, until the oscillation nearly fills the entire space between the rotating disks. This prediction is in qualitative agreement with the flow visualization observations of Humphrey and Gor.[15] Inspection of Figs. 5 and 6 shows that the cross-stream flow oscillations reach their maximum amplitude at $r/R_2=0.8$, approximately, and are constrained to the region of the flow that is not in solid-body rotation. The deviation from solid-body rotation is clearly indicated by the abrupt deflection of the circumferential velocity contours near $r/R_2=0.8$ on the rotating disk surface. The fairly delimited location of the oscillations is due to the need for the interdisk flow to evolve from an unsteady state of motion in the core to a state of solid-body rotation near the hub. This
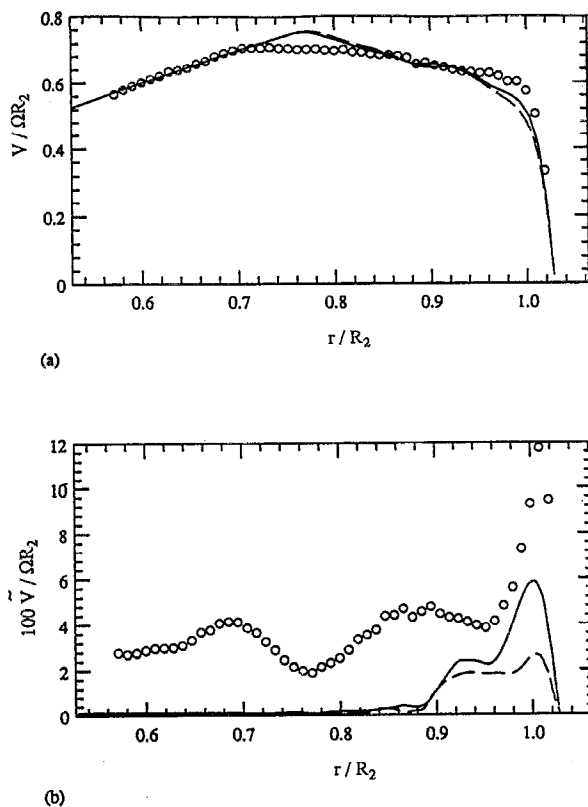
FIG. 8. Comparison between measurements (circles) and calculations (lines) of the circumferential velocity component (a) mean and (b) rms along the interdisk midplane for Re=22 200. (---) Two-dimensional calculations; (—) three-dimensional calculations.

the velocity rms by the two-dimensional calculation procedure, and the higher (numerical) value of the Reynolds number found for the transition to unsteady flow, can be attributed to several factors. First, the actual flow is three dimensional and, as shown in the figure and discussed below, the rms values increase significantly when a three-dimensional calculation is performed. Second, the thickness of the disks is ignored in the calculations. The tip of a disk represents an additional source of instability for the flow ejected radially outward in the Ekman layer. In addition, small but unavoidable imperfections in the disks, in the curvature of the enclosure wall, and in the relative orientation of various parts of the test section can induce perturbations in the experiment that result in higher rms and lower speed of rotation for transition to unsteady flow than calculated numerically. Finally, false numerical diffusion tends to stabilize the calculated flow, making necessary the use of unusually refined grids or higher-order difference schemes to counteract this effect. Schuler[4] shows that the truncation error of the QUICK interpolation scheme introduces an artificial numerical viscosity given by $\nu_{num} \approx \frac{1}{8}(\Delta\lambda)^2 \, \partial u_\lambda/\partial\lambda$, where $\Delta\lambda$ is the grid spacing and u_λ is the velocity component in the λ direction. Higher artificial viscosities are introduced by the upwind and central difference schemes, respectively. As shown in Sec. III A, the grid-dependent viscosity is small in the present two-dimensional calculations. Therefore, the inability of two-dimensional calculations to reproduce experimental rms results is primarily due to the dimensionally constrained numerical representation of the flow. While larger in the three-dimensional flow calculations discussed below, the grid-dependent viscosity does not affect the qualitative interpretation of those results.

This section concludes with an explanation for the cross-stream flow oscillations calculated when Re>22 200. Assume that at a particular instant in time the inward-directed radial jet is nearer the top disk, as shown in Fig. 6(b). As a result, fluid with a smaller circumferential component of momentum is brought closer to the top Ekman layer, increasing the axial gradient of circumferential velocity there. At the same time, since the jet is farther away from the lower disk, the gradient of circumferential velocity near the bottom Ekman layer decreases. Because the axial gradient of circumferential velocity determines the intensity of the radial flow in the Ekman layers, the radial flow in the top Ekman layer will increase, relative to that in the lower layer. This intensified radial flow is redirected axially along the enclosure wall to displace the stagnation point and the radial jet downward, toward the bottom disk. Once the jet is located below the geometrical symmetry plane, the same mechanism will operate in reverse to raise the jet.

C. Unsteady periodic three-dimensional flow

Unsteady three-dimensional calculations have been performed for the above flow configuration on a grid consisting of 32 planes uniformly spaced in the circumferential direction, each plane contains 31×41 nonuniformly distributed nodes to yield a total of $31 \times 41 \times 32$ $(n_r \times n_z \times n_\theta)$ nodes. (This grid required 8 Mbytes of on-line memory, and a typical run time ranged from 30 to 40 CPU hours on an Alliant

requires an intermediate fluid layer (shown as region III in Fig. 1), wherein, according to the Taylor–Proudman theorem, gradients in the direction parallel to the axis of rotation of all the velocity components are small. The result is the formation of a circumferential detached shear layer (the equivalent of a Taylor column) in which the present cross-stream motion is oscillatory in time and essentially parallel to the axis of rotation. This finding is discussed again, further below, in connection with the unsteady three-dimensional calculations.

Figure 7 shows time records of the three velocity components at $r/R_2 = 1$ on the interdisk midplane. (The scaling of the u and w velocity components in the figure is the appropriate one in this region of the flow.) As expected, the oscillation frequency of the radial and circumferential velocity components is twice that of the axial velocity component (u, v: 6.1 Hz; w: 3.05 Hz). The results in Figs. 6 and 7 support the arguments presented in Section III A to explain the differences between the measurements and calculations compared in Fig. 3.

Figure 8 compares unsteady two- and three-dimensional calculations of the mean and rms circumferential velocity components on the interdisk midplane, with corresponding measurements for Re=22 200. We focus here on the two-dimensional results. The mean velocity profiles are in reasonable agreement. However, although qualitatively similar, the calculated rms profile is significantly smaller in magnitude than the experimental profile. The underprediction of

supercomputer. More refined grids were not possible, due to on-line memory and computer speed limitations.) Although somewhat coarse in the circumferential direction, the cross-stream distribution of nodes ensured not less than five grid points in the disk and enclosure wall boundary layers. The estimated level of ν_{num}/ν incurred in these calculations ranges from about 0 near the hub to less than 1–5 near the enclosure wall, thus lowering the effective Reynolds numbers of the calculated flows.

In order to accelerate the transition to three-dimensional flow, a radially dependent oscillatory perturbation is added to the axial velocity boundary condition at $\theta=0$ along the top and bottom disks. The perturbation, given by $v_z'(r,t) = \Omega r 10^{-4} \sin(\Omega t)$, is intended to simulate a small wobbling motion in the rotating disks, and is introduced at $t=0$ for a very short time period. The magnitude of the perturbation is negligible relative to the amplitude of the axial velocity oscillations that ensue. This is verified by continuing the calculations with and without the perturbation present. Calculations are performed for two rotation rates corresponding to Re=22 200 and 44 400 ($\Omega_r=300$ and 600 rpm). Both sets of results are available in Schuler,[4] but here we focus primarily on the main findings for Re=44 400.

The starting condition for the calculation at Re=22 200 is the steady, axisymmetric solution obtained at Re=14 800. The flow remains two dimensional (axisymmetric) until $\Omega_r t/60=5$, approximately, when it experiences a transition to an unsteady three-dimensional pattern. Subsequently, the initially axisymmetric distribution of axial vorticity on the interdisk midplane gradually evolves into a series of nodes or foci with high values of this vorticity component. However, by $\Omega_r t/60=25$, the frequencies predicted for the three velocity components (u,v: 11.0 Hz; w: 5.5 Hz) are already 80% larger than the values observed in the unsteady two-dimensional calculations, and four foci of intensified ω_z vorticity appear in the flow.

Midplane radial profiles of the mean and rms circumferential velocity components derived from the three-dimensional calculations at Re=22 200 are plotted in Fig. 8. Also shown are the corresponding experimental measurements and two-dimensional calculations discussed earlier. While the differences between the two- and three-dimensional calculations of mean velocity are small, the latter show slightly better agreement with the measurements. The three-dimensional rms velocities show a more significant improvement over the two-dimensional results, especially near the fixed enclosure wall. Both the shape and magnitude of the three-dimensional rms profile are in better agreement with the experimental profile. Given the larger levels of artificial diffusion affecting the three-dimensional calculations, the improvement observed over the unsteady two-dimensional results must be attributed to resolving three-dimensional effects.

The result of imposing a step change in the disk speed of rotation, from Re=22 200 to 44 400, is shown in Fig. 9. As fluid near the disks accelerates, the axial gradient of the circumferential velocity increases and the cross-stream motion in the $r-z$ plane intensifies due to an increase in the radial component of motion in the Ekman layers. The initial effect
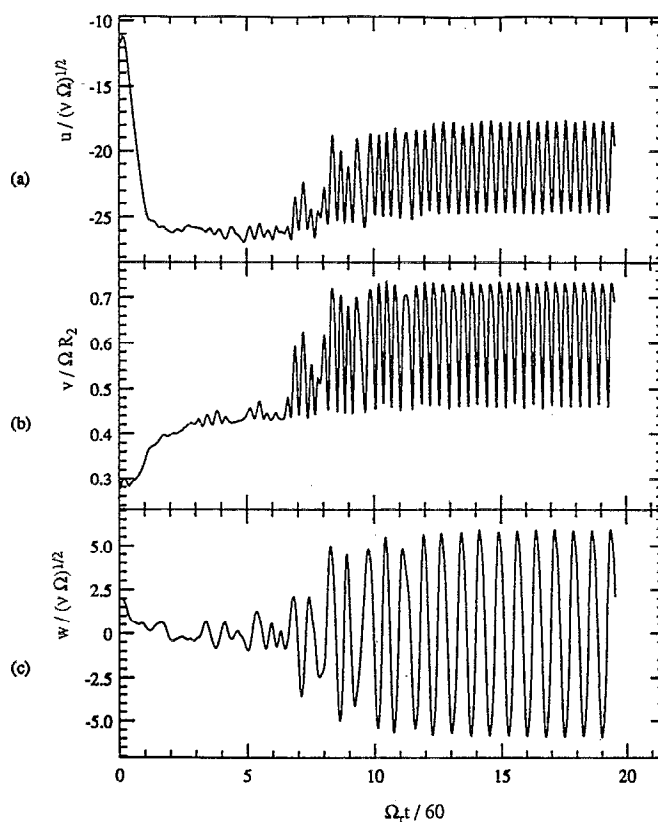

FIG. 9. Time variation of the three velocity components at $r/R_2=1$ on the interdisk midplane, obtained from three-dimensional calculations for Re =44 400 (600 rpm).

of the accelerating cross-stream flow is to dampen the amplitude of the interdisk jet oscillations. The dampening lasts until the flow in the core acquires its final unsteady-periodic velocity distribution, and a solid-body rotation region is re-established near the hub. Beyond about $\Omega_r t/60=3$ in Fig. 9, the jet oscillations reappear, and by $\Omega_r t/60=8-9$, an unsteady-periodic flow pattern similar to that obtained for Re=22 200 emerges. In the fully developed periodic state, the calculated velocity component frequencies are u, v: 26.7 Hz, and w: 13.35 Hz, respectively.

Figure 10 shows mean and rms radial distributions of circumferential velocity on the interdisk midplane for Re =44 400. In the absence of experimental results for this speed of rotation, the calculations are compared with corresponding velocity profiles measured by Schuler[4] at Re =22 200 and 88 800. Reasonable agreement is found between the measured and computed mean velocity profiles. The larger magnitude of the jet oscillations at Re=44 400 is responsible for the marked maximum in the calculated rms velocity profile near the enclosure wall. The periodic axially alternating entrainment of relatively fast moving fluid from regions near the disks into the slower moving core produces a local maximum in the calculated time-averaged velocity distribution near the enclosure wall. (This feature is also present in the experimental measurements of mean velocity shown in Fig. 3 for Re=7400 and 14 800.) The calculated rms profile is in qualitative agreement with the measure-
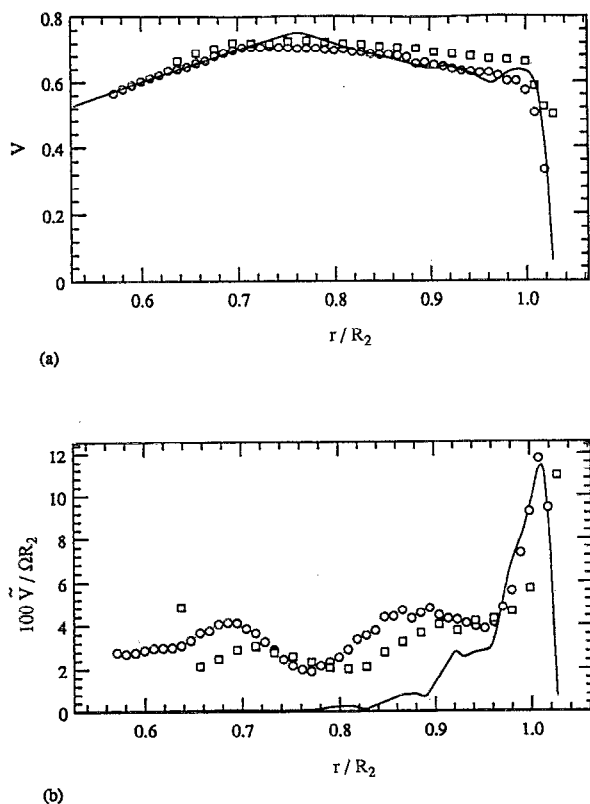
FIG. 10. Comparison between measurements (symbols) and three-dimensional calculations (line) of the circumferential velocity component (a) mean and (b) rms along the interdisk midplane. (—) three-dimensional calculations for Re=44 400 (600 rpm); experiments: (○) Re=22 200 (300 rpm), (□) Re=88 800 (1200 rpm).

ments near the enclosure wall, but significantly underpredicts the experimental data for $r/R_2 < 0.92$. As will be shown, the interdisk flow oscillations are strongly three dimensional, and the present underprediction of the rms velocity is partly due to the coarseness of the grid in the circumferential direction.

Plots of the r-z plane cross-stream vector velocity field for the same instant in time, $\Omega_r t/60 = 15$, at consecutive cross-stream planes are shown in Fig. 11 for the flow at Re=44 400. The oscillatory motion is similar to that predicted by the unsteady two-dimensional calculation at Re =22 200. However, there is a major difference between the two- and three-dimensional results: the oscillations in the three-dimensional case are functions of both the circumferential (θ) location and time, while the oscillations in the axisymmetric case have been constrained to be a function of time only. Note that relative to the pattern at $\theta=0°$, that at $\theta=60°$ appears to be shifted and inverted. Although not shown, the pattern at $\theta=0°$ reappears at $\theta=120°$. The calculated alternating change in sign of the axial velocity component in the detached shear layer, region III in Fig. 1, is in agreement with the cross-stream flow visualization results of Humphrey and Gor.[15] The calculations also reveal the existence of very weak secondary motions embedded in region IV, the region of solid-body rotation near the hub.

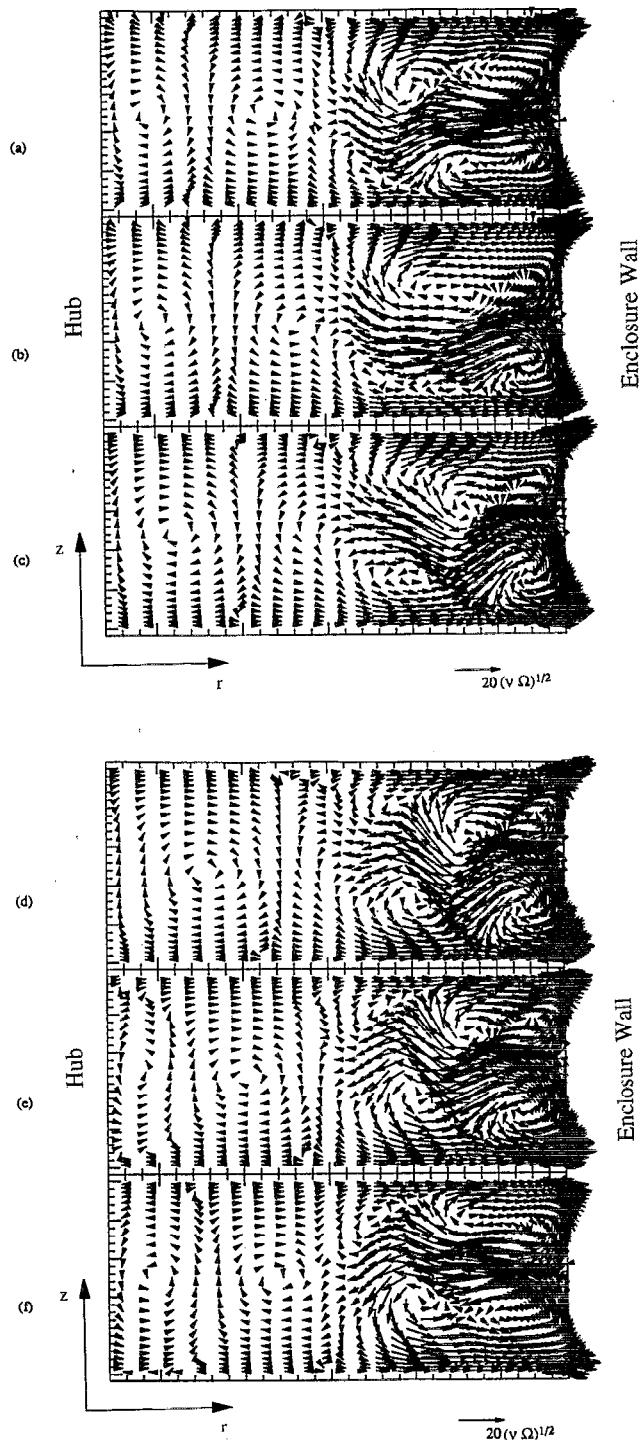FIG. 11. Plots of the cross-stream vector velocity field from three-dimensional calculations for Re=44 400 at $\Omega_r t/60 = 15$: (a) $\theta=0°$, (b) 12°, (c) 24°, (d) 36°, (e) 48°, and (f) 60°. The insert at the bottom of the figure provides a scale for the vectors in the plots.

D. A model for the unsteady periodic three-dimensional flow

Even though tainted by false diffusion, the present three-dimensional calculations confirm some and help explain other important features of the flow between corotating disks in axisymmetric enclosures. Instantaneous contours of the
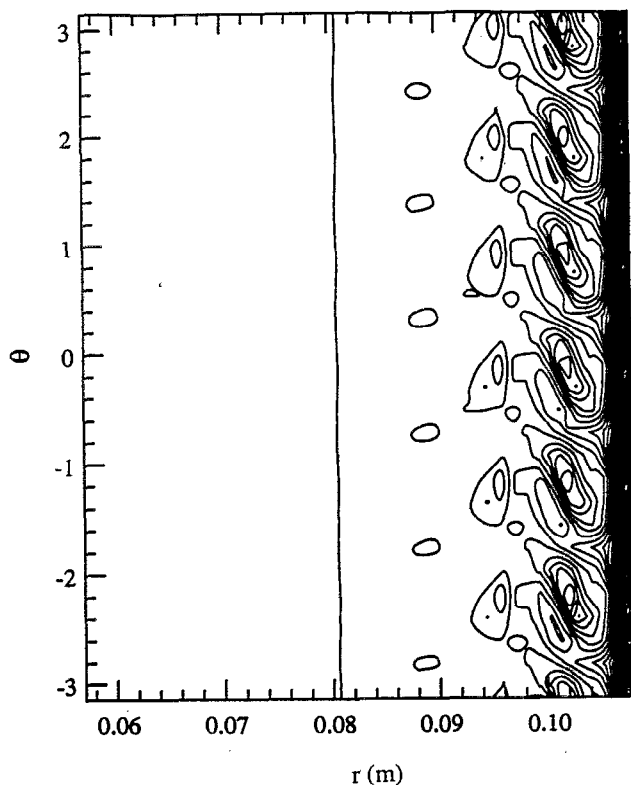
FIG. 12. Isocontours of the axial vorticity component, ω_z, on the interdisk midplane from three-dimensional calculations for Re=44 400 at $\Omega_r t / 60 = 15$. Note that $\omega_z = 2\Omega$ in the region of solid-body rotation to the left of the straight line in the figure.
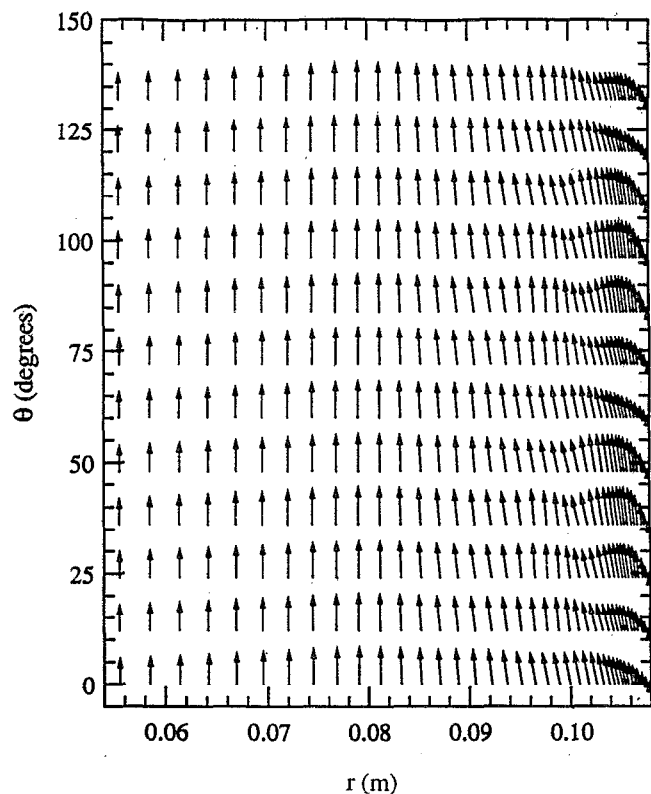
FIG. 13. Plot of the interdisk midplane vector velocities for the conditions of Fig. 12. The radial profiles correspond to circumferential locations spaced 12° apart. The vector velocity at the hub serves as a reference value.

midplane distribution of the axial vorticity component, ω_z, are plotted in Fig. 12 for the developed flow at Re=44 400. The nodal pattern in the figure, observed from a fixed frame of reference, is similar to that visualized by Abrahamson et al.[13,14] from a rotating frame of reference. Attention is now directed to an interpretation of the nodal distribution of ω_z. For the purpose of discussion, the numerical values of the ω_z contours in Fig. 12 are not important. We simply note that $\omega_z \approx \partial v / \partial r + v / r$ is a good approximation in the present flow.

The interpretation of the nodal distribution of ω_z in Fig. 12 is facilitated by reference to Fig. 13, which shows radial distributions of the vector velocity contained in the interdisk midplane at 12° intervals for the same instant in time. The profiles show that near the enclosure wall, $v / r \to 0$ and $\partial v / \partial r$ becomes large and negative. As a result, ω_z is also large and negative in this region. The profiles maximize ($\partial v / \partial r \to 0$) a short distance of order $\delta_E = (v / \Omega)^{1/2}$ from the enclosure wall, where, because $v / r > 0$, ω_z is now positive. Inboard of this radial location $\partial v / \partial r \geq 0$ and ω_z remains positive, maximizing periodically in the θ direction at those locations, where $\partial v / \partial r$ is largest. These observations are correctly reflected in the ω_z contours plotted in Fig. 12. The contours reveal a dark band of negative ω_z vorticity in a region of thickness δ_E adjacent to the enclosure wall, and a nodal distribution of positive ω_z vorticity inboard of the band. The nodes consist of six foci of intensified ω_z vorticity, separated

in the circumferential direction by smaller, but still positive, values. The region of flow in solid-body rotation, where $\omega_z = 2\Omega$, is separated from the three-dimensional core by the edge of the detached shear layer at $r / R_2 = 0.77$, corresponding to $r \approx 0.08$ m in the figure.

It is now helpful to consider the circumferential variation of the axial velocity component, w, associated with the nodal distribution of ω_z vorticity shown in Fig. 12 and the circumferential velocity component, v, contributing to the vectors in Fig. 13. For this we first note from Figs. 6 and 11 that periodic axial deflections of the inward-directed radial jet (which originates about the midplane by the enclosure wall) lead to periodic *increases* of the v velocity on the midplane near the enclosure wall, due to the displacement away from the midplane of fluid with relatively low circumferential momentum. This is fully supported by the velocity time records in Fig. 9, calculated on the midplane at $r / R_2 = 1$, which show that the maxima in the v velocity oscillation coincide, alternately, with the maximum (positive) and minimum (negative) values of the w velocity oscillation. Correspondingly, the minima in the v velocity oscillation coincide with the zero values of the w velocity oscillation. It is clear, therefore, that a node of concentrated positive ω_z vorticity coincides with a region of flow, where the v velocity component maximizes in the circumferential direction due to the w velocity component acquiring a maximum (positive) *or* a minimum (negative) value.
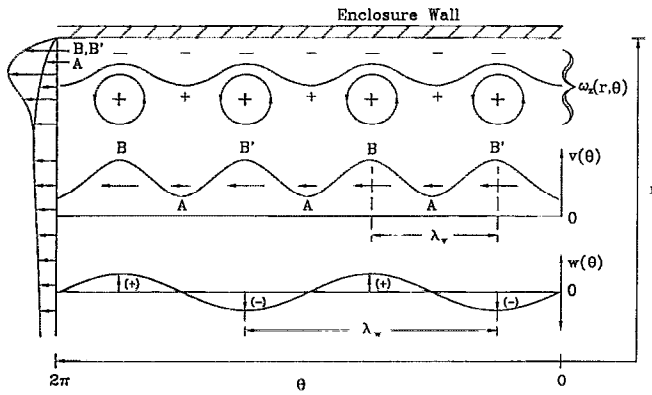
FIG. 14. Idealized schematic of the near-wall axial vorticity (ω_z) distribution on the midplane between a pair of disks corotating in a fixed cylindrical enclosure for conditions of three-dimensional unsteady flow. Also shown are typical circumferential (θ) variations of the axial (w) and circumferential (v) velocity components in this region of flow. The points labeled B and B' correspond to locally asymmetric cross-stream flow patterns, of the type shown in Figs. 6(b) and 6(c). The points labeled A correspond to locally symmetric cross-stream flow patterns, of the type shown in Fig. 6(a). Note that $2\pi/\lambda_w = n$ ($=1,2,3,...$) is an integer and that $2\pi/\lambda_v = 2n$ ($=2,4,6,...$) is always an even integer. All quantities are shown relative to a fixed frame of reference.

Figure 14 schematically illustrates the arguments presented in the above two paragraphs. It is a highly idealized schematic of the midplane region of flow near the curved enclosure wall at a fixed instant in time. For a flow moving from right to left, the figure shows (i) the near-wall (r-θ) variation of ω_z vorticity, including the circumferentially distributed foci; (ii) typical θ variations of the circumferential, v, and axial, w, velocity components in this region of flow; (iii) typical r variations of the v velocity component corresponding to the maximum (B,B') and minimum (A) points on the $v(\theta)$ profile. The B and B' maxima coincide with instantaneous, locally asymmetric cross-stream flow patterns, of the type shown in Figs. 6(b) and 6(c). The A minima coincide with instantaneous, locally symmetric flow patterns, of the type shown in Fig. 6(a).

Figure 14 emphasizes the following points: (a) very near the enclosure wall, the ω_z vorticity is everywhere negative and large; (b) inboard of this region $\partial v/\partial r \to 0$ and $v/r > 0$ producing positive ω_z vorticity; (c) the positive ω_z vorticity is further intensified at nodes, in the regions of flow (B,B'), where $\partial v/\partial r > 0$; and (d) the B and B' maxima in the $v(\theta)$ profile coincide with maximum positive and negative values, respectively, of the $w(\theta)$ profile. As a result, $\lambda_w = 2\lambda_v$, where λ is the oscillation wavelength of the particular velocity component.

From these results, it is clear that the presence of circumferentially periodic foci of intensified ω_z vorticity is intimately connected to the (r,θ) variation of the v velocity component, and that the θ variation of v is linked to the θ variation of the w velocity component. The θ variation of w consists in periodic reversals of this velocity component, which explains the experimentally observed alternations in sign of the axial component of motion of the detached shear layer in this flow. Thus, the connection postulated in Hum-

phrey and Gor[15] between periodic oscillations of the present cross-stream flow and the circumferentially distributed foci of axial vorticity is conclusively established.

The profile for $w(\theta)$ in Fig. 14, characterizing the near-wall circumferential variation of the axial velocity component, is periodic with wavelength λ_w, such that $2\pi/\lambda_w = n$ is an integer. Since the wavelength of the circumferential velocity component is $\lambda_v = \lambda_w/2$, it follows that $2\pi/\lambda_v = 2n$, and we conclude that the number of v velocity component waves in the near-wall interdisk space is always even. Because the maxima (B,B') of this wave coincide with the locations of the ω_z vorticity nodes, we conclude that the number of those nodes about the interdisk midplane is also always even.

As explained in Sec. I A 1, the data for the Strouhal number ($\mathrm{St} = 60f/\Omega_r$) presented in Fig. 2 were obtained from time records of the v velocity component measured on the midplane near the enclosure wall. Recognizing that the frequency f is common to both the v velocity and ω_z vorticity, it is easy to show that $\mathrm{St} = 2\pi f/\Omega$ and $2n = 2\pi f/\Omega_F$, where Ω_F is the angular velocity of the foci. The data in Fig. 2 show stepwise changes of St of order unity ($\Delta\mathrm{St} \approx 1$). If we make the reasonable assumption that these changes correspond to jumps in n equal to unity ($\Delta n = 1$), then it follows that

$$\frac{\Omega_F}{\Omega} = \frac{\Delta\mathrm{St}}{2\,\Delta n} \approx \frac{1}{2}. \tag{14}$$

This relation states that for the experimental conditions of Fig. 2, ranging from $\mathrm{Re} = 4440$ to $266\,400$, the angular velocity of the ω_z nodes is very close to half that of the disks. We next consider the numerical and experimental support for this finding.

From the v velocity data in Fig. 9 for the three-dimensional flow calculated at $\mathrm{Re} = 44\,400$, it follows that the time difference between two consecutive maxima is $\Delta t \approx (26.7)^{-1}$ s. Since, as shown in Fig. 12, there are $2n = 6$ foci of ω_z vorticity in this flow, and since these foci coincide with the v velocity maxima, it follows that $\Omega_F/\Omega \approx 0.44$. A similar analysis of the data in Schuler[4] for the (prematurely terminated) three-dimensional flow calculated at $\mathrm{Re} = 22\,000$ yields $\Omega_F/\Omega \approx 0.55$ for $2n = 4$ foci observed at $\Omega_r t/60 = 25$. These numerically based estimates are within $\pm 12\%$ of the results given by Eq. (14).

From the measured radial profiles of the time-averaged v velocity component provided in Fig. 2 in Schuler et al.[1] it is possible to estimate the ratio Ω_F/Ω over the range $22\,200 < \mathrm{Re} < 266\,400$. For this, we note that

$$\frac{\Omega_F}{\Omega} = \frac{\Omega_F}{\Omega} \times \frac{r_F}{r_F} = \frac{V_F}{V_D}, \tag{15}$$

where V_F is the circumferential velocity component of the foci rotating at a radius r_F and V_D is the corresponding velocity of the disks at the same radius. Taking $r_F/R_2 \approx 1$ as the approximate radial location of the foci, and assuming that the value of V_F is close to the average circumferential velocity of the surrounding flow, the data in Schuler[4] yield $\Omega_F/\Omega = V_F/V_D = 0.60 \pm 0.04$. This estimate is also in reasonable agreement with the result given by Eq. (14).

In similar rotating disk flow experiments, Lennemann[11] and Abrahamson et al.,[13,14] respectively report $\Omega_F/\Omega \approx 0.8$ and 0.75. Except for the interdisk spacing, H/R_2, there is close geometrical and dynamical similarity between their respective experiments and the present flow configuration. Here, however, $H/R_2 = 0.091$, while $H/R_2 = 0.04$ in Lennemann[11] and $H/R_2 = 0.05$ in Abrahamson et al.[13,14] That decreasing H/R_2 at fixed Re should increase Ω_F/Ω is expected, since decreasing the interdisk spacing favors a viscous merging of the disk Ekman Layers, and the radial expansion of the flow region in solid-body rotation. For experimental evidence of the latter, see Fig. 4(a) in Humphrey and Gor.[15]

Given that $2n = \text{St } \Omega/\Omega_F$, setting $\Omega/\Omega_F = 2$ from Eq. (14) yields $2n = 2$ St for the experimental conditions of Fig. 2. From this we conclude that the number of ω_z foci on the interdisk midplane varies from 12 to 4 over the Reynolds number range considered in the experiment of Schuler.[4] In particular, for values of Re slightly less than 44 400, the number of foci is $2n = 10$, while for values slightly larger than 44 400 the number is $2n = 8$. The calculations corresponding to Re=44 400 yield $2n = 6$. The lower number of foci predicted numerically is attributed to insufficient grid refinement to completely resolve the spatial structure of the flow.[36]

It is important to note that the total number, $2n$, of ω_z foci numerically predicted on the interdisk midplane will not be revealed by an experiment that visualizes the region of flow associated with only one of the two toroidal vortices between the disks. If, for example, colored dye is preferentially injected into one of the two interdisk half-spaces, and if the diffusion of dye is slow compared to convection (a condition favored by nonturbulent flows), only half of the $2n$ foci will be clearly seen in an axially projected view of the interdisk space. It is not clear from the descriptions in the studies of Lennemann[11] and Abrahamson et al.[13,14] that such a bias was avoided (or did not arise) in their flow visualization experiments. (Abrahamson[37] has subsequently communicated that in his experiments the acid-base indicator dye was evenly distributed in the interdisk space.) The fact that they respectively observed uneven as well as even numbers of foci in well-behaved flows at relatively low speeds of rotation suggests: (a) that the flow visualization techniques (based on the use of aluminum powder and bromothymol blue, respectively) in both cases may have emphasized a view of the events associated primarily with one of the two toroids in the interdisk space; (b) and/or that transition modes of motion consisting of uneven numbers of midplane foci may have been observed by these investigators.

IV. CONCLUSIONS

Two- and three-dimensional calculations performed for the unsteady laminar flow between a pair of disks corotating in a fixed cylindrical enclosure provide new insight for the interpretation of experimental observations and the improved understanding of this class of flows. While three-dimensional calculations show better overall qualitative agreement with the experimental results available than the two dimensional, both sets of calculations reveal an instability in the region

near the curved enclosure wall, where the disk Ekman layers turn to collide against each other. As a result, the inward-directed radial jet that forms between the initially symmetrical pair of counter-rotating toroidal vortices begins to oscillate in the cross-stream plane for Re$\geq$22 200 ($\Omega_r \geq 300$ rpm). The corresponding experimental value for this instability is Re$\geq$4400 ($\Omega_r \geq 60$ rpm). Uncontrolled perturbations in the experiments and numerical diffusion in the calculations are partly responsible for the differences in these results.

In agreement with present measurements and earlier flow visualization observations, the three-dimensional calculations reveal circumferentially periodic reversals of the axial velocity component, which induce circumferentially periodic accelerations and decelerations of the circumferential velocity component. This results in an even number of circumferentially periodic foci of intensified axial vorticity located on the interdisk midplane near the curved enclosure wall. Half of these nodes (nodes 1, 3, 5,...) are associated with one of the two cross-stream toroidal vortices, the other half (nodes 2, 4, 6,...) are associated with the other toroidal vortex.

Analysis of present experimental data in light of the numerical results shows that for an interdisk spacing $H/R_2 = 0.091$, the number of foci can vary from 12 at low speeds of rotation (Re<22 200) to 4 at high speeds of rotation (Re<266 400). It is also found that the ratio of the angular velocity of the foci to that of the disks is essentially constant, $\Omega_F/\Omega \sim \frac{1}{2}$, over the range of Re explored (4440–266 400). The data available for other flow configurations very similar geometrically to the present one show that Ω_F/Ω increases with decreasing H/R_2. This is attributed to the increased importance of viscous effects with decreased interdisk spacing.

The question arises as to the physical meaning of the odd number of foci observed in the flow visualization experiments of, for example, Abrahamson et al.[13,14] At least two explanations are possible. First, their dye visualization technique may have emphasized a view of the events associated primarily with the structure of the flow in one-half of the interdisk space; that is, associated primarily with one cross-stream toroidal vortex and its corresponding ω_z foci. Second, although three-dimensional calculations presented here reveal well-behaved streamlined, space- and time-periodic flow fields for Re=22 200 and 44 400, the results are stabilized by numerical diffusion. It is conceivable that finer grids, especially for calculations with larger values of Re and H/R_2, would uncover more disorganized or chaotic states of motion, with sporadic mergings and spontaneous regenerations of ω_z foci. Under such conditions, the even "$2n$" integer rule uncovered in the present investigation may not apply.

The wavy vortex flow pattern revealed by the present three-dimensional calculations resembles, at least superficially, the wavy patterns discussed in the literature dealing with the instabilities of Taylor vortices in circular Couette flow[38] and Dean vortices in curved channel flow.[39] Using the notation of Fig. 1 and defining a radius of curvature by $R_c = (R_1 + R_2)/2$, investigations performed in these two configurations have generally been for geometries with $(R_2 - R_1)/H \ll 1$ and $(R_2 - R_1)/R_c \ll 1$; that is, corresponding

Humphrey, Schuler, and Webster

to flows in very narrow but wide and mildly curved passages with negligible end wall effects. In contrast, in the present configuration $(R_2-R_1)/H=5.1$ and $(R_2-R_1)/R_c=0.6$, with the consequence that fluid motion in the interdisk space is dominated by the combined effects of the rotating disk and fixed enclosure wall boundary layers. Notwithstanding, it is of interest to consider some similarities and dissimilarities among the three flows. (1) In all three cases, the transition from steady to wavy vortex motion occurs at a specific value of a characteristic dimensionless parameter: the Taylor, Dean, or Reynolds number. (2) The angular velocity of the periodic traveling wave is less than some characteristic velocity: in the case of Taylor vortices it tends to about one-third of the inner cylinder angular velocity; in the case of Dean vortices it is less than the maximum streamwise fluid velocity; in the present flow it is about half the disk angular velocity; and in all three cases it depends only weakly on the Reynolds number. (3) As in the case of Taylor and Dean wavy vortex flows, present cross-stream $(r-z)$ plane vector velocity patterns appear to be shift-and-reflect symmetric. In this regard, it is readily shown that the continuity and momentum equations, as well as the boundary conditions describing the present flow, satisfy the shift-and-reflect symmetry conditions given in, for example, Finlay et al.[39] (4) The wavelengths of Taylor and "twisting-type"[39] Dean instabilities decrease with increasing Reynolds number; the wavelengths of "undulating-type"[39] Dean instabilities first increase and then decrease with increasing Reynolds number; the wavelength of the present traveling wave instability increases with increasing Reynolds number. (5) The waviness in Taylor and Dean vortex flows results from nonaxisymmetric disturbances that are $\pi/2$ out of phase in the spanwise (z-coordinate) direction and that are circumferentially or streamwise periodic. However, in the present flow configuration motion of the fluid in the z-coordinate direction is limited by the solid disks. (6) While the origin of wavy Taylor and "undulating-type" Dean vortex flows is probably due to a secondary centrifugal instability, that for "twisting-type" Dean vortex flow is attributed to a secondary shear instability.[39] The shear instability is associated with two inflection points in the circumferential velocity profile (v plotted as a function of z at fixed r), located at $z=1/4\lambda$ and $3/4\lambda$, respectively, where λ is the spanwise wavelength of a Dean vortex pair in a curved channel. It is most interesting that the z profile of the time-averaged circumferential velocity, V, measured at $r/R_2=1.0$ in the present flow with Re $=22\,200$, shows the presence of inflection points at $z=0.24H$ and $0.74H$, approximately; see Fig. 3(a) of Schuler et al.[1]

In conclusion, except for the variation in wavelength as a function of Reynolds number, the present flow shares various important characteristics with wavy Taylor and Dean vortex flows. In particular, we suggest that the transition from a steady two-dimensional flow to an unsteady three-dimensional wavy flow may be due to a secondary shear instability of the type postulated by Finlay et al.[39] for Dean vortex flow. The proof of this requires a stability analysis beyond the scope of the investigation.

[1] C. A. Schuler, W. R. Usry, B. Weber, J. A. C. Humphrey, and R. Greif, "On the flow in the unobstructed space between shrouded corotating disks," Phys. Fluids A **2**, 1760 (1990).

[2] C. J. Chang, C. A. Schuler, J. A. C. Humphrey, and R. Greif, "Flow and heat transfer in the space between two corotating disks in an axisymmetric enclosure," J. Heat Transfer **111**, 625 (1989).

[3] C. J. Chang, J. A. C. Humphrey, and R. Greif, "Calculation of turbulent convection between corotating disks in axisymmetric enclosures," Int. J. Heat Mass Transfer **33**, 2701 (1990).

[4] C. A. Schuler, "Investigation of the flow between rotating disks in an enclosure," Ph.D. thesis, University of California, Berkeley, 1990.

[5] H.-M. Tzeng and J. E. Fromm, "Airflow study in a cylindrical enclosure containing multiple corotating disks," IBM Res. Report No. RJ7334, 1990.

[6] J. A. C. Humphrey, C. J. Chang, H. Li, and C. A. Schuler, "Unobstructed and obstructed rotating disk flows: A summary review relevant to information storage systems," Adv. Information Storage Syst. **1**, 79 (1991).

[7] H.-M. Tzeng and J. A. C. Humphrey, "Corotating disk flow in an axisymmetric enclosure with and without a bluff body," Int. J. Heat Fluid Flow **12**, 184 (1991).

[8] H.-M. Tzeng and C. J. Chang, "Obstructed flow between shrouded corotating disks," Phys. Fluids A **3**, 484 (1991).

[9] J. A. C. Humphrey, C. A. Schuler, and I. Iglesias, "Analysis of viscous dissipation in disk storage systems and similar flow configurations," Phys. Fluids A **4**, 1415 (1992).

[10] D. Gor, J. A. C. Humphrey, and R. Greif, "Ventilated flow in the unobstructed space between corotating disks in a cylindrical enclosure," J. Fluid Eng. **115**, 398 (1993).

[11] E. Lennemann, "Aerodynamic aspects of disk files," IBM J. Res. Dev. **18**, 480 (1974).

[12] D. G. Akhmetov and V. F. Tarasov, "Structure and evolution of vortex cores," J. Appl. Mech. Tech. Phys. **27**, 690 (1987).

[13] S. D. Abrahamson, D. Koga, and J. E. Eaton, "An experimental investigation of the flow between shrouded corotating disks," Report No. MD-50, Thermoscience Division, Department of Mechanical Engineering, Stanford University, 1988.

[14] S. D. Abrahamson, J. E. Eaton, and D. Koga, "The flow between shrouded corotating disks," Phys. Fluids A **1**, 241 (1989).

[15] J. A. C. Humphrey and D. Gor, "Experimental observations of an unsteady detached shear layer in enclosed corotating disk flow," Phys. Fluids A **5**, 2438 (1993).

[16] J. E. Fromm, "A numerical study of unstable flow between rotating disks," IBM Res. Report No. RJ4734, 1985.

[17] J. E. Fromm, "Understanding turbulence through Navier–Stokes computation of flow between rotating disks," IBM Research Report No. RJ5999, 1987.

[18] C. A. Schuler, E. B. Treidler, and J. A. C. Humphrey, "CUTEFLOWS (Computing Unsteady Three-Dimensional Elliptic Flows): A user's guide," University of California at Berkeley, Computer Mechanics Laboratory Report No. 91-001, 1991.

[19] P. LeQuere, J. A. C. Humphrey, and F. S. Sherman, "Numerical calculation of thermally driven two-dimensional unsteady laminar flow in cavities of rectangular cross section," Num. Heat Transfer **4**, 249 (1981).

[20] M. P. Arnal, D. J. Goering, and J. A. C. Humphrey, "Unsteady laminar

flow developing in a curved duct," Int. J. Heat Fluid Flow **13**, 347 (1992).

[21] S. V. Patankar, *Numerical Heat Transfer and Fluid Flow*, Series in Computational Methods in Mechanics and Thermal Sciences (Hemisphere, New York, 1980).

[22] F. H. Harlow and J. E. Welch, "Numerical calculation of time-dependent viscous incompressible flow of fluid with free surface," Phys. Fluids **8**, 2182 (1965).

[23] B. P. Leonard, "A stable and accurate convective modeling procedure based on quadratic upstream interpolation," Comput. Methods Appl. Mech. Eng. **19**, 59 (1979).

[24] A. J. Chorin, "A numerical method for solving incompressible viscous flow problems," J. Comput. Phys. **2**, 12 (1967).

[25] A. J. Chorin and J. E. Marsden, *A Mathematical Introduction to Fluid Mechanics* (Springer-Verlag, New York, 1979).

[26] P. K. Khosla and S. G. Rubin, "A conjugate gradient iterative method," Comput. Fluids **9**, 109 (1981).

[27] H. L. Stone, "Iterative solution of implicit approximations of multidimensional partial differential equations," SIAM J. Num. Anal. **5**, 530 (1968).

[28] D. S. Kershaw, "The incomplete Cholesky-conjugate gradient method for the iterative solution of system of linear equations," J. Comput. Phys. **26**, 43 (1978).

[29] D. G. Luenberger, *Linear and Nonlinear Programming* (Addison–Wesley, Reading, MA, 1984).

[30] R. Peyret and T. D. Taylor, *Computational Methods for Fluid Flow* (Springer-Verlag, New York, 1983).

[31] E. B. Treidler, "An experimental and numerical investigation of flow past ribs in a channel," Ph.D. thesis, University of California, Berkeley, 1991.

[32] K. Tatsutani, R. Devarakonda, and J. A. C. Humphrey, "Unsteady flow and heat transfer for cylinder pairs in a channel," Int. J. Heat Mass Transfer **36**, 3311 (1993).

[33] A. Z. Szeri, S. J. Schneider, and F. Labbe, "Flow between rotating disks. Part I. Basic Flow," J. Fluid Mech. **134**, 103 (1983).

[34] K. Tatsutani, W. R. Usry, and J. A. C. Humphrey, "Numerical calculation of two-dimensional laminar flow and heat transfer for a backward-facing step using CUTEFLOWS" in *Benchmark Problems for Heat Transfer Codes*, ASME Winter Annual Meeting, HTD-Vol. 222, edited by B. F. Blackwell and D. W. Pepper, Anaheim, CA 8–13 November 1992, pp. 1–6.

[35] I. Iglesias, J. A. C. Humphrey, and F. Giralt, "Numerical calculation of two-dimensional buoyancy-assisted flow past a backward-facing step in a vertical channel," in *Computational Aspects of Heat Transfer, Benchmark Problems*, ASME Winter Annual Meeting, HTD-Vol. 258, edited by B. F. Blackwell and B. F. Armaly, New Orleans, LA November 28–December 3, 1993, pp. 63–72.

[36] Herrero (personal communication, 1994). Limited calculations subsequently performed with the same numerical algorithm and for the same flow configuration (with $a/H=0$) on a grid with 74 $\times 40 \times 52$ ($n_r \times n_z \times n_\theta$) nodes yield $2n=8$.

[37] S. D. Abrahamson (personal communication, 1994).

[38] A. Davey, R. C. Di Prima, and J. T. Stuart, "On the instability of Taylor vortices," J. Fluid Mech. **31**, 17 (1968).

[39] W. H. Finlay, J. B. Keller, and J. H. Ferziger, "Instability and transition in curved channel flow," J. Fluid Mech. **194**, 417 (1988).